

SUPERBIT SCIENCE POTENTIAL & 2019 FLIGHT HARDWARE INTEGRATION

by

Mohamed Shaaban

A thesis submitted in conformity with the requirements
for the degree of MSc Option 1
Graduate Department of Physics
University of Toronto

Abstract

SuperBIT Science Potential & 2019 Flight Hardware Integration

Mohamed Shaaban

MSc Option 1

Graduate Department of Physics

University of Toronto

2019

Contents

1	Introduction	1
1.1	Astronomy From the Stratosphere	1
1.2	Super-pressure Balloon-borne Imaging Telescope (SuperBIT)	1
2	Science Background	4
2.1	Overview	4
2.2	Preliminaries	5
2.2.1	Standard Model of Cosmology	5
2.2.2	Bending of Light	6
2.2.3	Weak Lensing Formalism	7
2.3	Measuring Shear (Images to Catalogs)	10
2.4	Catalogs to Science	13
2.4.1	Convergence Power Spectrum	13
2.4.2	Cosmic Shear	13
2.5	Systematics	14
3	BIT 2019 Flight Hardware Integration	16
3.1	Overview	16
3.2	Computer & Electronic Upgrades	16
3.3	UFO System	18
3.4	Secondary Motors	19
3.5	Baffle Mounting Device	19
3.6	Battery Boxes	20
3.7	Inner Frame Design	20
	Bibliography	20

Chapter 1

Introduction

The purpose of this report is to provide a general and pedagogical higher level understanding of SuperBIT. The report structure is as follows; I begin by providing an overview of the instrument and how it operates. I then present the the reader with the theoretical background necessary to understand the forecasted data analysis process as well as appreciate the challenges SuperBIT needs to overcome. Finally, I summaries some of my personal contributions to the instrument in the context of the upcoming September 2019 flight.

1.1 Astronomy From the Stratosphere

Collecting astronomical data from the stratosphere via a balloon borne instrument presents a plethora of advantages many of which are unique to ballooning. As seen in Figure 1.1 an optical telescope operating in the stratosphere can observe radiation more efficiently than ground based observatories, this is especially true in the blue and near UV frequency range. Additionally, such an instrument would operate above significant atmospheric turbulence and can thus provide diffraction-limited resolutions. While a space based telescope can similarly address the shortcomings of ground based observations, launching a propellant-based vehicle is 100-1000 times more expensive. Given the relative low cost of ballooning and the short development timescale of balloon borne instruments, ballooning uniquely provides the opportunity of an iterative development process relying on multiple test flights to ensure smooth scientific operation. The instrument of interest in this report namely, SuperBIT is a balloon borne imaging telescope designed to utilize the advantages listed above.

1.2 Super-pressure Balloon-borne Imaging Telescope (SuperBIT)

SuperBIT is an optical to near UV balloon borne half meter telescope providing diffraction-limited 0.25 arcsecond resolution imaging over a 0.4 degree field of view with sensitivities exceeding 24th magnitude in 300 seconds of integration. SuperBIT is designed for an ultra-long duration balloon (ULDB) 100 day flight with the immediate science goal of providing precision weak and strong lensing mass measurements for more than 150 clusters. Diffraction limited resolution requires stable pointing, in the case of SuperBIT the goal is to point with a stability of 20 milliarc-seconds. This pointing is achieved in two distinct stages,

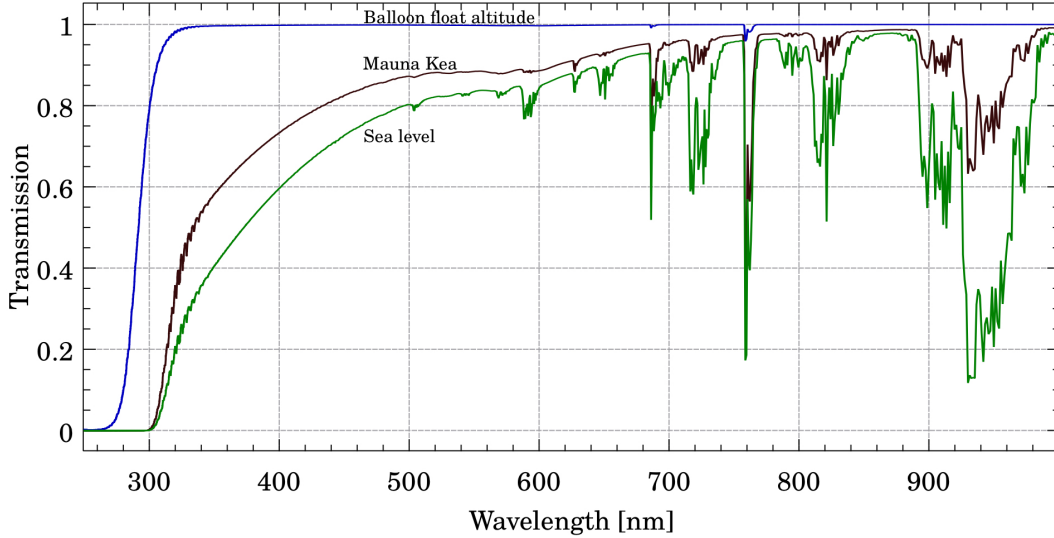


Figure 1.1: Transmission of the atmosphere vs wavelength at sea level (green), Mauna Kea (brown), and balloon float altitude (blue). It is clear that a balloon borne optical telescope provides a significant increase in exposure in the blue and near UV frequency range.

the first stage is stabilizing the gondola (seen in Figure 1.2) in three axes with a peak-to-peak accuracy of better than an arc-second in the presence of external motions at the several arc-minute level. This stabilization is achieved using stepper motors correcting for the motions in each euler angle by moving superBIT's three frames; the outer frame moving in yaw, the middle frame moving in roll, and the inner frame moving in pitch. Gyroscopes and a two star camera system are used as the motion feedback for the motor's correction. The second stage is achieving sub-arcsecond pointing via the fine guidance optical system (seen in Figure 1.3). The optical system uses a 0.5 meter class modified dall kirkham telescope for light collection that is then fed into an optics box. In the optics box part of the field of view is picked off by a pick off mirror and fed to a high speed camera, the high speed camera uses the position of a bright star to provide information on the sub arcsecond motion of the gondola that is corrected for by a tip tilt mirror. This tip/tilt correction results in sub arc-second stabilization from the perspective of the science camera located at the end of the optical path.

For a more detailed description of the instrument please consult group alumni theses. For details on the electrical distribution systems and superBIT mechatronics please see John Hartley's PhD thesis, for the mechanical structure see Steven Lis Engineering Masters Thesis, for a detailed discussion of the controls system and software see Javier Romualdez's PhD Thesis, for a detailed look at the star cameras system see Matthew Galloway's PhD Thesis, and for details of the thermal control system see Susan Redmonds Engineering Masters Theses.

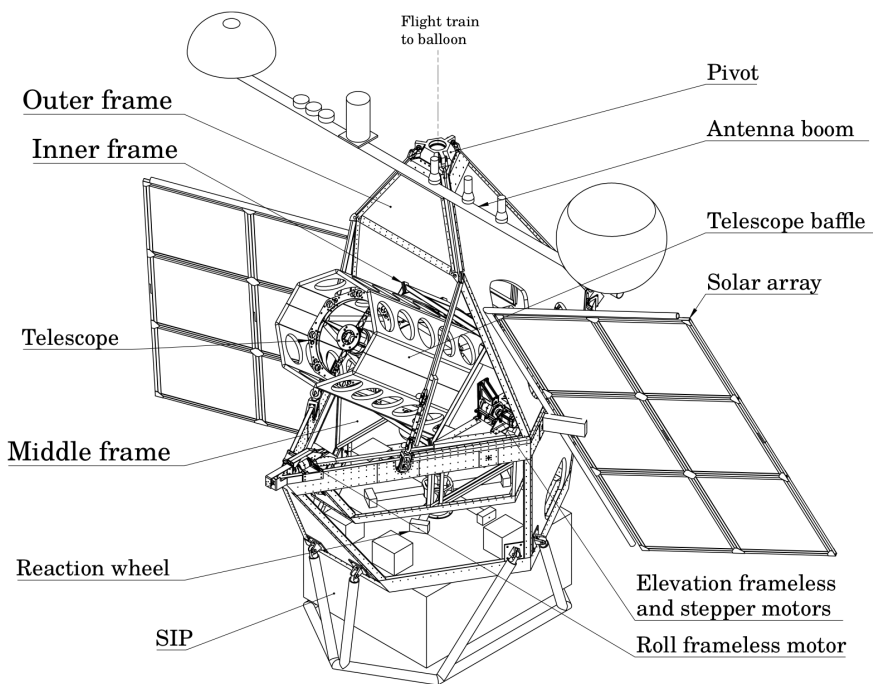


Figure 1.2: Layout of the SuperBIT instrument.

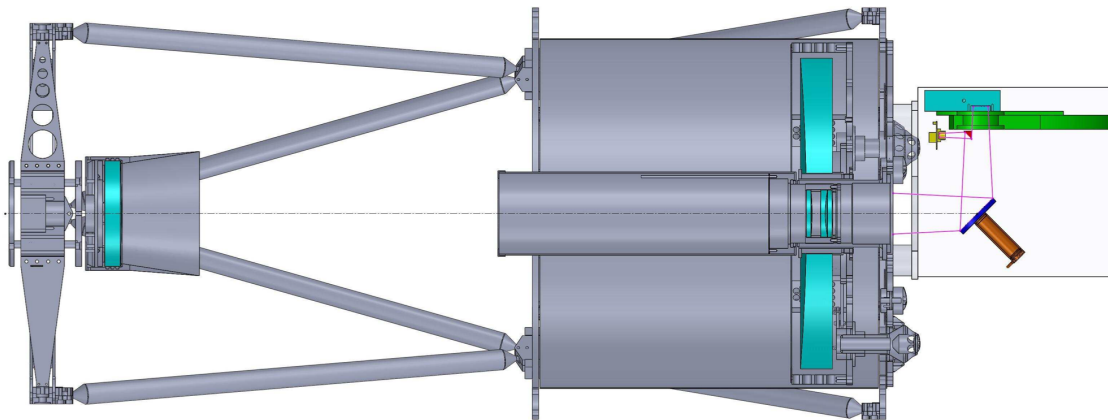


Figure 1.3: The optical layout; The optical path (violet lines) is fed into the fine guidance system through the telescope (grey). The Tip/Tilt mirror (gold and blue) redirects the optical axis 90 degrees to the Science camera (cyan) through a filter wheel (green). Just before the filter wheel some of the light is redirected again by the pick-off mirror (red) to a star camera (yellow).

Chapter 2

Science Background

2.1 Overview

The most revolutionary discovery in cosmology since Hubble observed that the Universe is expanding is that this expansion is accelerating. A revelation that was awarded the 2011 Nobel Prize for its profound implications. [1]. An accelerating universe implies that either our understanding of gravity is flawed or that a mysterious negative pressure known as Dark Energy is driving the expansion [14]. This Dark Energy accounts for most (over 68%) of the energy density in the observable universe, however its origin and physics are presently unknown [2]. As a result, the nature of Dark Energy is considered one of the greatest mysteries of modern science [3].

One of the most powerful ways to probe Dark Energy, as well as modified theories of gravity, is a technique known as weak gravitational lensing, or weak lensing for short [7, 10]. Gravitational lensing is the phenomenon of light ray deflection by intervening mass. When the deflection is sufficiently weak, this phenomenon manifests in images of galaxies as a shearing effect due to the differential deflection of neighboring light rays [18, 7]. This shearing induces a subtle (sub 1%) change in the ellipticity of the images. Although such a change is negligible in comparison to the 30% dispersion in intrinsic galaxy ellipticities, it can be statistically measured by using the coherence of the lensing shear over the sky [18]. The reason weak lensing is considered very powerful is because it provides a direct measurement of the matter distribution in the universe as a function of redshift independent of any cosmological assumptions. Thus, allowing us to directly probe the growth of cosmic structure with time [7]. (Add in the case of superbit we will be doing cluster count)

In this section I present a general overview of weak lensing in the context of cosmology. I begin by presenting the theory behind the Cosmology we would like to probe, as well as the general theoretical framework on which weak lensing operates. I then present the weak lensing measurement procedure and how cosmological data can be extracted from such measurements in generality. Finally, I end this section with a short discussion on potentially concerning systematics that will need to be addressed in analysis.

2.2 Preliminaries

2.2.1 Standard Model of Cosmology

The fundamental assumption in cosmology, known as the cosmological principle, is that we live in a homogenous (independent of position) and isotropic (independent of direction) universe [18, 16]. Solving Einstein's equations under the geometric symmetries provided by the cosmological principle and taking into account the expansion of the universe one finds that the dynamics of the universe are governed by the Friedman equation [16, 18],

$$H^2(z) = H_0^2 \left(\Omega_r(1+z)^4 + \Omega_m(1+z)^3 + \Omega_k(1+z)^2 + \Omega_\Lambda \frac{\rho_\Lambda(z)}{\rho_\Lambda(0)} \right) \quad (2.1)$$

were H is hubble's constant, z is the redshift, and Ω_i is the normalized energy density of radiation, matter, space-time curvature, and Dark Energy at $z = 0$. The parameter ρ_Λ is theoretically predicted to be a constant, however, this prediction is yet to be experimentally confirmed as the evolution of Dark Energy is experimentally unconstrained [18]. There have been a variety of methods proposed to probe this evolution, those methods are summarized in [5, 18]. In essence all the probes simplify to the same concept; one uses an observable to track a cosmological distance as a function of redshift. Due to report size constraints distance measures in cosmology will not be discussed in this report. For a complete summary of cosmological distances see [8]. Within the standard model of cosmology we expect energy density evolution to behave as follows

$$\frac{\rho_i(z)}{\rho_i(0)} = (1+z)^{3(1+w)} \quad (2.2)$$

therefore, for dark energy to be a constant it requires $w = -1$. Thus, probing dark energy evolution in the simplest case amounts to constraining the parameter w . The probe of interest in this report, namely weak lensing, relays on the ability of cosmological theories to predict the large scale distribution of matter.

Matter Distribution

The standard model predicts that quantum fluctuations in the early universe became macroscopic due to inflation, and proceeded to act as gravitational seeds for the formation of large scale structure in the universe [17, 18, 16]. The gravitational evolution of those fluctuations follows linear perturbation theory [18]. The amplitude of the fluctuations is given by the density contrast

$$\delta(\vec{x}, t) = \frac{\rho_m(\vec{x}, t) - \langle \rho_m(t) \rangle}{\langle \rho_m(t) \rangle} = \delta(\vec{x}, t_0) \frac{G(t)}{G(t_0)} \quad (2.3)$$

were t_0 is some arbitrarily chosen initial time and $G(t)$ is the linear growth function obeying the differential equation

$$\ddot{G} + 2H(z)\dot{G} - \frac{3}{2}\Omega_m H_0^2(1+z)^3 G = 0 \quad (2.4)$$

The solution to this equation can only be written in integral form for specific forms of H , and thus specifying $\rho_\Lambda(z)$ [18, 16]. Finally, we note that the central limit theorem ensures that the distribution is a gaussian random field and therefore the statistical properties of the distribution are completely

described by its power spectrum P_δ . In the limit where $\delta \ll 1$ the power spectrum can be separated into a product between the linear growth function G and a shape function,

$$P_\delta(k) = \sigma_8^2 G(t)^2 \mathcal{P}(k) \quad (2.5)$$

where \mathcal{P} is a slowly varying shape function and σ_8 is defined as

$$\sigma_8 = \int_0^\infty \frac{k^2 dk}{2\pi} P_\delta(k) W_8(k) \quad (2.6)$$

Therefore, σ_8 is the present root-mean-square matter fluctuation averaged over a sphere of radius $8h^{-1}$ Mpc, this is physically interpreted as parametrization of how strongly the matter is clumped.

To summarize, the evolution of dark energy directly influences the large scale distribution of matter, and the distribution's statistical properties are fully described by its power spectrum. Therefore, if we can directly measure the power spectrum of the matter distribution a likelihood analysis can be performed to constrain the evolution of dark energy.

2.2.2 Bending of Light

The fundamental concept on which weak lensing is built is gravity's ability to alter the path of a photon. This phenomenon is explored in full detail in [15, 9, 12]. In this subsection I present a simple overview of the theory behind the bending of light necessary to develop the weak lensing formalism. For more detailed calculations consult [15, 9, 12].

Newtonian Lens

It is a common misconception that the gravitational bending of light is an exclusive property of GR. However, gravity induced alterations to a photon's path are predicted by newtonian mechanics [13]. To illustrate this consider a mass M located at the origin of the cartesian plane and a corpuscle(newtonian photon) propagating along the $x = b$ line (in this context b is known as the impact parameter). Newton's second law predicts that the presence of the point mass will result in a momentum transfer between the two objects. If the corpuscle starts with momentum $(p, 0)$ then it will end up with momentum (p_x, p_y) . Therefore, the particle path is deflected by some angle $\hat{\alpha}$. The deflection angle is simply given by

$$\sin(\hat{\alpha}) = \frac{p_y}{\sqrt{p_x^2 + p_y^2}} \quad (2.7)$$

For very small deflections we have $p \approx p_x \gg p_y$ and $\hat{\alpha} \ll 1$. Therefore Equation 2.7 simplifies to $\hat{\alpha} \approx \frac{p_y}{p_x}$. We now consider the infinitesimal deflection along the entire path of the photon with $d\hat{\alpha} = \frac{dp_y}{p_x} = \frac{1}{p_x} dx \frac{dp_y}{dx}$. Therefore, we can find the deflection angle by

$$\begin{aligned} \hat{\alpha}_N &= -\frac{1}{p_x} \int dx \frac{dp_y}{dx} \\ &= -\frac{1}{cp_x} \int dx \frac{dp_y}{dt} \\ &= \frac{2GM}{c^2 b} \end{aligned} \quad (2.8)$$

We note that the mass of the corpuscle cancels out of the deflection equation. Therefore this equation applies for massless particles i.e. photons. Therefore Equation 2.8 provides a newtonian description for the bending of light [13].

General Relativistic Bending of Light

The Einstein's field equations in the presence of a charge free static point mass is uniquely solved by the Schwarzschild metric [15]. The Schwarzschild metric is

$$ds^2 = \left(1 - \frac{r_s}{r}\right) dt^2 - \left(1 - \frac{r_s}{r}\right)^{-1} dr^2 - r^2 d\Omega^2 \quad (2.9)$$

where r_s is the Schwarzschild radius of the system given by $r_s = 2\mu = 2GM/c^2$ and (t, r, Ω) are the standard parameters for 4D space-time in polar coordinates. We can analyze the path of the photon from section 2.2.2 by studying the geodesic equations of the metric and finding the conserved quantities of the system. We can then combine the conservation equations with the tangent vector norm condition for a null path to get the shape equation of the system as

$$\frac{d\phi}{dr} = \frac{1}{r^2} \left(\frac{1}{b^2} - \frac{1}{r^2} \left(1 - \frac{2\mu}{r}\right) \right)^{-1/2} \quad (2.10)$$

where (r, ϕ) are the photons position in 2D polar coordinates and b is the impact parameter. Rewriting this equation under the transformation of $r = 1/u$ and working perturbatively around $u(\mu = 0) = \frac{1}{b} \sin \phi$ we get

$$u(\phi) \approx \frac{1}{b} \sin \phi + \frac{3\mu}{2b^2} \left(1 + \frac{1}{3} \cos 2\phi\right) \quad (2.11)$$

in the limit where $\phi \ll 1$ and $u \rightarrow 0$ Equation 2.11 simplifies to $\phi = \hat{\alpha}_N = \frac{2GM}{c^2 b}$. Geometrically the deflection is given by $\hat{\alpha} = 2\phi$ and therefore the deflection angle is

$$\hat{\alpha} = 2\hat{\alpha}_N = \frac{4GM}{c^2 b} \quad (2.12)$$

We conclude that general relativity predicts a factor of 2 greater deflection form a point mass than is predicted by newtonian mechanics. This relationship greatly simplifies the formalism developed for weak lensing.

2.2.3 Weak Lensing Formalism

Now that we have a theoretical understanding of the Cosmological parameters we would like to measure, as well as an understanding of how gravitational fields impact the trajectory of light. We are ready to develop the theoretical formalism on which all weak lensing applications are built. This formalism is based on a combination of the frameworks developed in these sources [9, 18, 10, 7, 11, 12, 6].

Weak thin lens

In order to develop our formalism let us consider a general lensing system as seen in Figure 2.1. For astronomical applications on cosmological scales the distance from the observer to the lens D_L , the distance from the lens to the source D_{LS} , and the distance from the observer to the source D_S are much

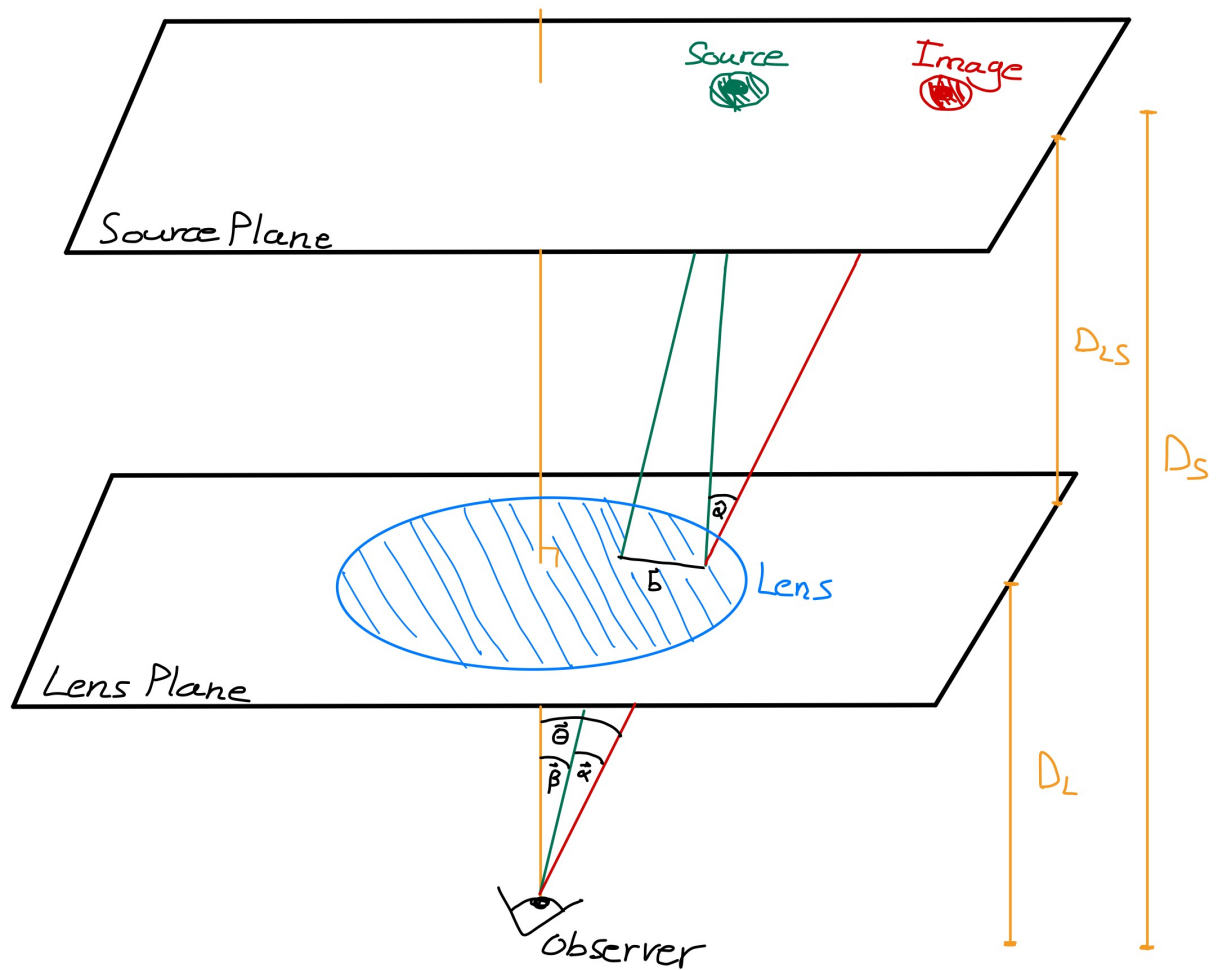


Figure 2.1: Sketch of a thin lens system highlighting the parameters of relevance in the weak lensing formalism. It is conventional to assume the planes are orthogonal to the z axis.

greater than the thickness of the lens along the optical axis. Therefore we can treat the lens as a "thin lens", i.e. it lives on a planar slice (lensing plane) along the line of sight. We project the mass and potential of the lens onto the lensing plane by defining the projected surface density Σ and projected potential Φ as

$$\begin{aligned}\Sigma(x, y) &= \int \rho(x, y, z) dz \\ \Phi &= \int \phi dz\end{aligned}\tag{2.13}$$

were ρ and ϕ are the spatial mass density and the newtonian potential respectively. We can now use the results from the previous section to find the deflection angle $\hat{\alpha}$ due to the extended thin lens. The deflection is given by

$$\hat{\alpha} = \frac{2}{c^2} \nabla \Phi(x, y)\tag{2.14}$$

were the factor of 2 comes from Equation 2.12 and ∇ is the two dimensional gradient. Note that this equation is equivalent to that describing the deflection of light by an optical lens with refractive index $n = 1 - 2\Phi/c^2$, hence the name lensing. Geometrically we have $\beta = \theta - \alpha$ and $\hat{\alpha} = \frac{D_{LS}}{D_S} \alpha$ from Figure 2.1. This leads us to the ray trace equation

$$\beta = \theta - \frac{D_{LS}}{D_S} \hat{\alpha}(\theta)\tag{2.15}$$

The ray trace equation is the fundamental equation in weak lensing relating all the geometric properties of the system to one another.

Differential deflection of adjacent light rays

In the weak limit the actual deflections are not observable because the true position of the source is unknown. As a result, only the effects of differential deflection can be measured. Two adjacent light rays from the source pass through the lens at slightly different positions and will therefore be deflected differently. This effect results in a remapping of the observed surface brightness of the source I_s to the observed surface brightness I_{obs} . This mapping can be linearized and is therefore given by

$$I_{obs}(\vec{\theta}) \approx I_s(A\vec{\theta})\tag{2.16}$$

were A is the Jacobian of the transformation. A convenient convention is to rewrite the 2D Jacobian as

$$A = \delta_{ij} - \frac{\partial^2 \Phi}{\partial \theta_i \partial \theta_j} = \begin{pmatrix} 1 - \kappa - \gamma_+ & -\gamma_\times \\ -\gamma_\times & 1 - \kappa + \gamma_+ \end{pmatrix}\tag{2.17}$$

were we have defined the convergence κ shear $\gamma = \gamma_+ + i\gamma_\times$ as

$$\begin{aligned}\kappa &= \frac{1}{2}(\partial_x^2\Phi + \partial_y^2\Phi) \\ \gamma_+ &= \frac{1}{2}(\partial_x^2\Phi - \partial_y^2\Phi) \\ \gamma_\times &= \partial_x\partial_y\Phi\end{aligned}\tag{2.18}$$

We can now study the geometric implications of the remapping. If we consider a circular source we see that γ_+ and γ_\times correspond to a stretching of the circle along the x/y axis and the $x=y$ line respectively, κ corresponds to isotropic enlargement of the source's profile, and since the mapping conserves surface brightness we observe an increase of the total flux by a magnification factor

$$\mu = \frac{1}{\det A} = \frac{1}{(1-\kappa)^2 - \gamma_+^2 - \gamma_\times^2}\tag{2.19}$$

these geometric effects are illustrated in Figure 2.2. To be more specific a circular source is mapped to an ellipse with major axis $a = (1 - \kappa - |\gamma|)^{-1}$ and minor axis $b = (1 - \kappa + |\gamma|)^{-1}$ [11]. If we define the reduced shear as $g = \gamma/(1 - \kappa)$ then an ellipse with ellipticity ϵ_{orig} is mapped to an ellipse with ellipticity ϵ_{obs} given by

$$\epsilon_{obs} = \frac{\epsilon_{orig} + g}{1 + g^*\epsilon_{orig}} \approx \epsilon_{orig} + \gamma\tag{2.20}$$

the approximate relationship is a result of the weak limit ($\kappa \ll 1$). Equation 2.20 and Equation 2.18 demonstrate that by measuring the apparent shapes of lensed objects we are measuring information about the lensing potential and hence the matter overdensity [10, 6, 7]. Equation 2.20 indicates that a population of intrinsically round sources ($\epsilon_{orig} = 0$) would be ideal, but unfortunately real galaxies have an average intrinsic ellipticity of 0.25 per component [6]. Instead the lensing signal is inferred by averaging over an ensemble of sources, under the assumption that the unlensed orientations are random [10, 6]. In the next section we talk about how such measurements are made.

2.3 Measuring Shear (Images to Catalogs)

The weak lensing analysis process can be conceptually split into two parts; 1) converting images to catalogs of galaxy shapes and 2) extracting scientific results from shape catalogs. In this section we present a sample image to catalog pipeline. An overview of a weaklensing analysis pipeline is presented in Figure 2.3.

Object Detection

The first step in weak lensing analysis is to detect the objects that will be analyzed. In the case of cosmological data the objects of interest are faint distant galaxies. Traditional methods for galaxy detection simply involve the detection of peaks above some detection threshold in a long exposure image. However due to the subtlety of the weak lensing signal the process is more involved. First we must confidently distinguish stars from galaxies, this is a fairly straight forward process that is usually done with photometric data. The next step is to detect galaxies that have blended together in the

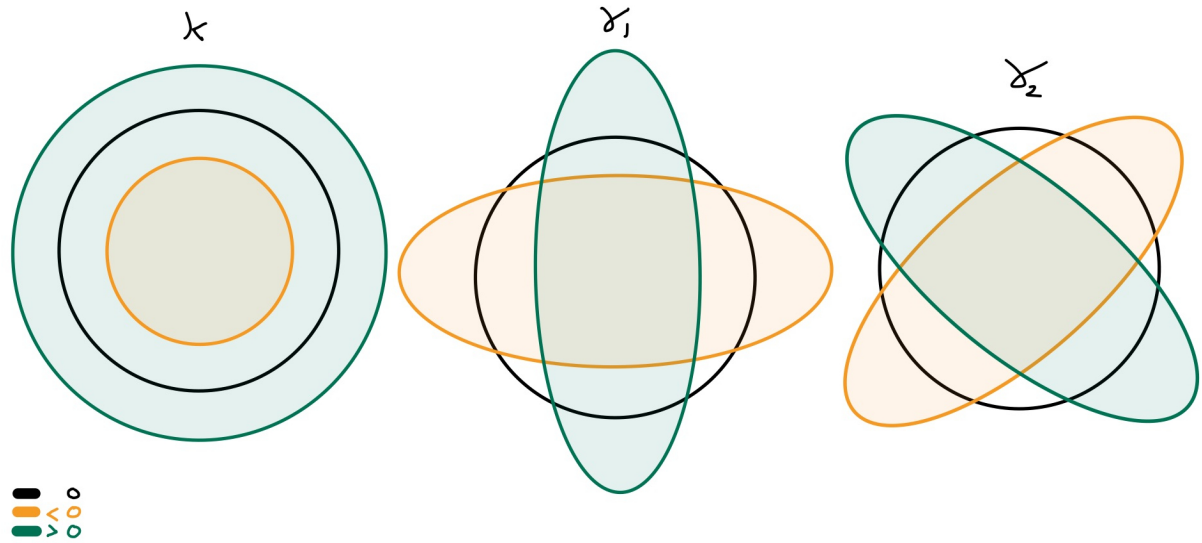


Figure 2.2: The effects of the convergence κ and the shear γ on a circular image of a galaxy. The black line represents the nominal image, orange represents positive parameter values, and green represents negative parameter values.

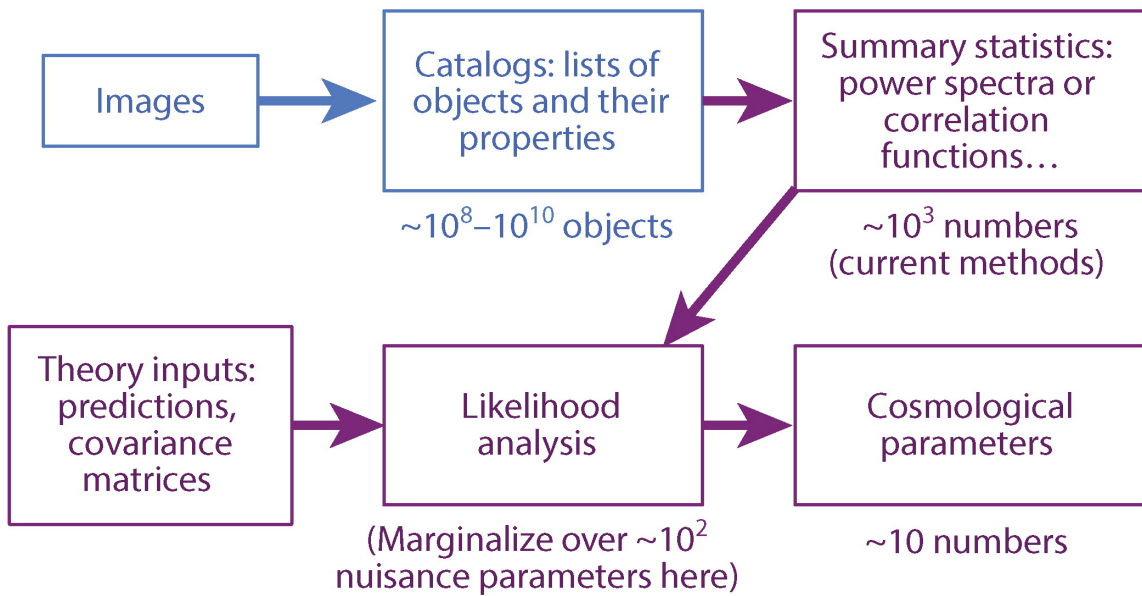


Figure 2.3: A generic outline of weak lensing pipeline analysis as presented in [10]. Note this is a cosmic shear pipeline and therefore is not identical to what a SuperBIT pipeline would look like. In the case of cluster count applications an additional block of mass calculations would be needed.

imaging process, i.e. detections with a double peak feature. Such blended images account for upto 10% of detections and therefore need to be either deblended or discarded from the data set [10, 18]. Finally, based on the systematics of the detector some selection criteria is introduced that will filter out problematic images.

Alternatively, another way galaxies are detected in images is by a likelihood analysis comparing imaged brightness profiles I to theoretical brightness profiles predicted by galactic theories.

Shape Extraction

After the galaxies are detected their shapes need to be measured. The accurate measurement of galaxy shape from an image is a rich and complex topic, we will state some results from [11, 18] without derivation. Galaxy shapes can be quantified by computing the second moments of the galaxy images

$$Q_{ij} = \frac{\int d^2x I(\vec{x}) W(\vec{x}) x_i x_j}{\int d^2x I(\vec{x}) W(\vec{x})} \quad (2.21)$$

were I is the brightness profile defined in Equation 2.16 and W is a weighting function introduced to effectively limit the domain of the integral. The exact relationship between the the second moments and ellipticity is convention dependant, in this section we will use the same definitions as [10, 6]. The size R and complex ellipticity ϵ are given by

$$R^2 = Q_{11} + Q_{22} \quad (2.22)$$

$$\epsilon = \frac{Q_{11} - Q_{22} + 2iQ_{12}}{Q_{11} + Q_{22}} \quad (2.23)$$

All ellipticity definitions have a well-defined response to a lensing shear and, hence, recover the same science after averaging across ensembles of galaxies. Equation 2.20 tells us that averaging over a randomly oriented galaxies gives us the mean shear ($\langle \epsilon \rangle = \langle \epsilon_{orig} \rangle + \langle \gamma \rangle = \langle \gamma \rangle$) and therefore an accurate measurement of ϵ suffices for statistical analysis.

Note that if the alternative object detection method is used, i.e. model fitting, then the ellipticity can be simply read off the best fit model without the need for computing second moments.

Point Spread Function

The point spread function (PSF) describes the response of an imaging system to a point source or point object. In practice the surface brightness profile of an object in an image is not the I_{obs} from Equation 2.16 but is convoloved with some unknown function $PSF(\vec{x})$. Therefore, in order to detect weak lensing signal we must understand and reconstruct our PSF in order to deconvolve it from the image. Deconvolving the PSF is the most important and most difficult step of any weak lensing analysis [6, 10]. The PSF has a width which leads to rounder images and typically is anisotropic, which leads to a preferred orientation. The bias is grouped into two kinds: a multiplicative bias m that scales the shear, and an additive bias c that reflects preferred orientations that are introduced. The observed shear and true shear are thus related by

$$\gamma_{obs} = (1 + m)\gamma + c \quad (2.24)$$

In order to take this effect the PSF must be accurately estimated and deconvolved from the results. This is done by observing a large field of stars and recording the optical systems response to a star as a function of position. The function is then estimated by interpolating between star positions.

2.4 Catalogs to Science

After we have measured galaxy shapes to the necessary accuracy we need to extract cosmological results from the data. More specifically we want to be able to extract the density contrast power spectrum discussed in the Section 2.

2.4.1 Convergence Power Spectrum

We first note that in the weak limit we can use the 3D newtonian comoving poisson equation

$$\nabla^2 \phi = \frac{3H_0^2 \Omega_m}{2a} \delta \quad (2.25)$$

were δ is the density contrast defined in Equation 2.3. Therefore, we can rewrite the convergence as

$$\kappa = \frac{3H_0^2}{2c^2} \Omega_m \int_0^{\chi_s} d\chi \frac{\chi(\chi_s - \chi)}{\chi_s} \frac{\delta(\chi)}{a} \quad (2.26)$$

were χ is the comoving angular diameter distance and a is the scale factor. Equation 2.26 shows that the convergence is a projection of the density contrast with the weight function

$$w(\chi) = \frac{3H_0^2 \Omega_m \chi (\chi - \chi_s)}{2c^2 \chi_s a} \quad (2.27)$$

thus, the convergence power spectrum is determined by the integral over the line of sight of the density contrast power spectrum[6, 10, 4]. More specifically, the convergence power spectrum can be written using the parameters from Equation 2.5 as

$$C_\kappa(l) = \frac{9}{4} \left(\frac{H_0}{c} \right)^4 \Omega_m^2 \sigma_8^2 \int_0^{\chi_s} d\chi \left[\frac{G(t) \chi (\chi_s - \chi)^2}{a \chi_s} \right] \mathcal{P} \left(\frac{1}{\chi} \right) \quad (2.28)$$

Equation 2.28 shows that the shape of C_κ depends on the shape \mathcal{P} of the density contrast power spectrum and thus can be inferred from a measurement of the convergence power spectrum. The growth factor G can also be measured to give us information of on the evolution of structure growth with time. Finally, while we set out to measure the influence of dark energy on structure formation Equation 2.28 allows us to additionally constrain the cosmological parameters Ω_m and σ_8 up to a degeneracy. The degeneracy is physically interpreted as weak lensing inability to differentiate between low density highly clumped matter and weakly clumped high density matter [18, 4].

2.4.2 Cosmic Shear

In the previous subsection we showed that if we could measure the convergence power spectrum then we will have achieved our scientific goal. However, you might notice that we never discussed measuring convergence, we only explained shear measurements. The reason is that measuring the convergence is significantly more challenging than measuring the shear. But, it turns out that the convergence power

spectrum is identical to shear power spectrum, therefore, our shear data suffices. To prove the statement let us begin by taking the fourier transform of Equation 2.18, the result is

$$\begin{aligned} 2\hat{\kappa} &= -l^2 \hat{\Phi} \\ 2\hat{\gamma}_+ &= -(l_1^2 - l_2^2) \hat{\Phi} \\ \hat{\gamma}_\times &= -l_1 l_2 \hat{\Phi} \end{aligned} \quad (2.29)$$

were the hat indicates the fourier transform of the function. Equation 2.29 allows us to investigate the magnitude of the functions, we find that

$$4|\hat{\gamma}| = |\hat{\Phi}|^2 (l_1^2 + l_2^2)^2 = 4|\hat{\kappa}|^2 \quad (2.30)$$

The power spectrum of a gaussian field depends exclusively on the magnitude therefore Equation 2.30 shows that the shear power spectrum C_γ is the same as the convergence power spectrum C_κ [4, 6, 10, 18]. The shear power spectrum is simply the fourier transform of the two point correlation function given by

$$\xi_{ij} = \langle \gamma_i \cdot \gamma_j^* \rangle \quad (2.31)$$

were i and j are redshift bin indices. This two point correlation is the so called "cosmic shear" and is physically the correlation between shears separated by an angular mode on the sky, i.e. if some image distortion by lensing is measured in one particular direction the image distortion nearby should be more similar and thus more correlated than a distortion far away. For a more in depth discussion on cosmic shear please see [13, 18, 6, 4].

The above discussion is the extraction procedure for ideal data. Working with real data is more challenging and requires the development of more tools, due to report size constraints we will not be presenting any further analysis techniques.

2.5 Systematics

Finally, we end this report with a discussion with a topic almost synonymous with weak lensing, systematic errors. Weak lensing has proven the most technically challenging cosmological probe due to the large range of systematic errors it suffers from [18]. Below We present a very brief overview over the rich topic of weak lensing systematics, for more details please see [11, 18].

1. **PSF Errors:** As mentioned previously the PSF of the optical system needs to be estimated in order to extract meaningful data. This estimation involved interpolation between the systems response to a star, this interpolation is a less accurate representation of the PSF the further we get from a star. This uncertainty in the PSF could result in systematically introducing additional shear in a subset of the data and therefore detecting false signals.
2. **Blending:** As discussed previously approximately 10% of the galaxies observed have some form of blending. This introduces the following problem; we can be over aggressive with our blended object identification which could result in non blended objects being flagged as blended and unnecessarily tampered with or conversely we could be too lenient with our detection allowing blended objects

into our analysis. Both cases would introduce a systematic error into our data. Additionally, even if our detection algorithm is perfect our deblending algorithm might not be which would induce a systematic in 10% of the data.

3. **Selection Bias:** Depending on the optical system used to detect the galaxies an algorithm is needed to filter out unusable objects. The reason an object is unusable could stem from PSF uncertainty, blending, detector systematics or any other reason. Imperfections in such algorithms could result in an implicit shape dependance on the selection, such a dependance introduces/removes shear signal from the data.
4. **Intrinsic Alignment:** Finally, throughout this entire the report the fundamental assumption has been that galaxy orientations are randomly distributed. This assumption is not entirely true, factors such as proximity to other galaxies, angular momentum during formation, and location relative to the center of mass of a cluster all impact the alignment of galaxies. A good example of this is the fact that galaxies near the center of a cluster tend to be oriented in a manner such that they point towards the center[10].

Chapter 3

BIT 2019 Flight Hardware Integration

3.1 Overview

Before SuperBIT can collect scientific data it must fly! In this section I give a brief summary of some of my personal contributions to the hardware integration efforts for the upcoming 2019 flight. Due to page constraint of the report hardware images are kept to a minimum however such images are available upon request. More project write ups are also available upon request including data and summaries of software behavior.

3.2 Computer & Electronic Upgrades

A full schematic of the bit electronics and computer system can be found in Figure 3.1. Due to the complexity of the system it will not be described in detail, I will focus exclusively on the changes done for the 2019 flight. The first electronic project was updating the Main Control Computer (MCC), a MESA FPGA 4i69 board was added with a RS422 daughter board to read out the optical gyroscopes and the absolute encoders providing position of the gondola frames. The next change was done to the Inner Frame Computer (IFC), the actual cpu card was switched to a multi core lower power version of the old cpu. Additionally, similar to the MCC a MESA FPGA 4969 board was added to read out the quadrature encoders for the position of the telescopes secondary mirror. A serial card was removed and replaced by a USB hub for serial communications. Finally, a new Focal Plane Computer (FPC) needed to be built from scratch. The computer was built as an identical clone of the first FPC. The FPC is used to control the data from the pick-off mirror system, a second computer was added in order to add a second pick-off mirror for improved fine pointing. Other minor electronic upgrades included the installation of two new actuator controllers and a new thermistor readout box. Minor internal rewiring was done in the MCC and the IFC to allow for additional thermistor readout channels on the computers.

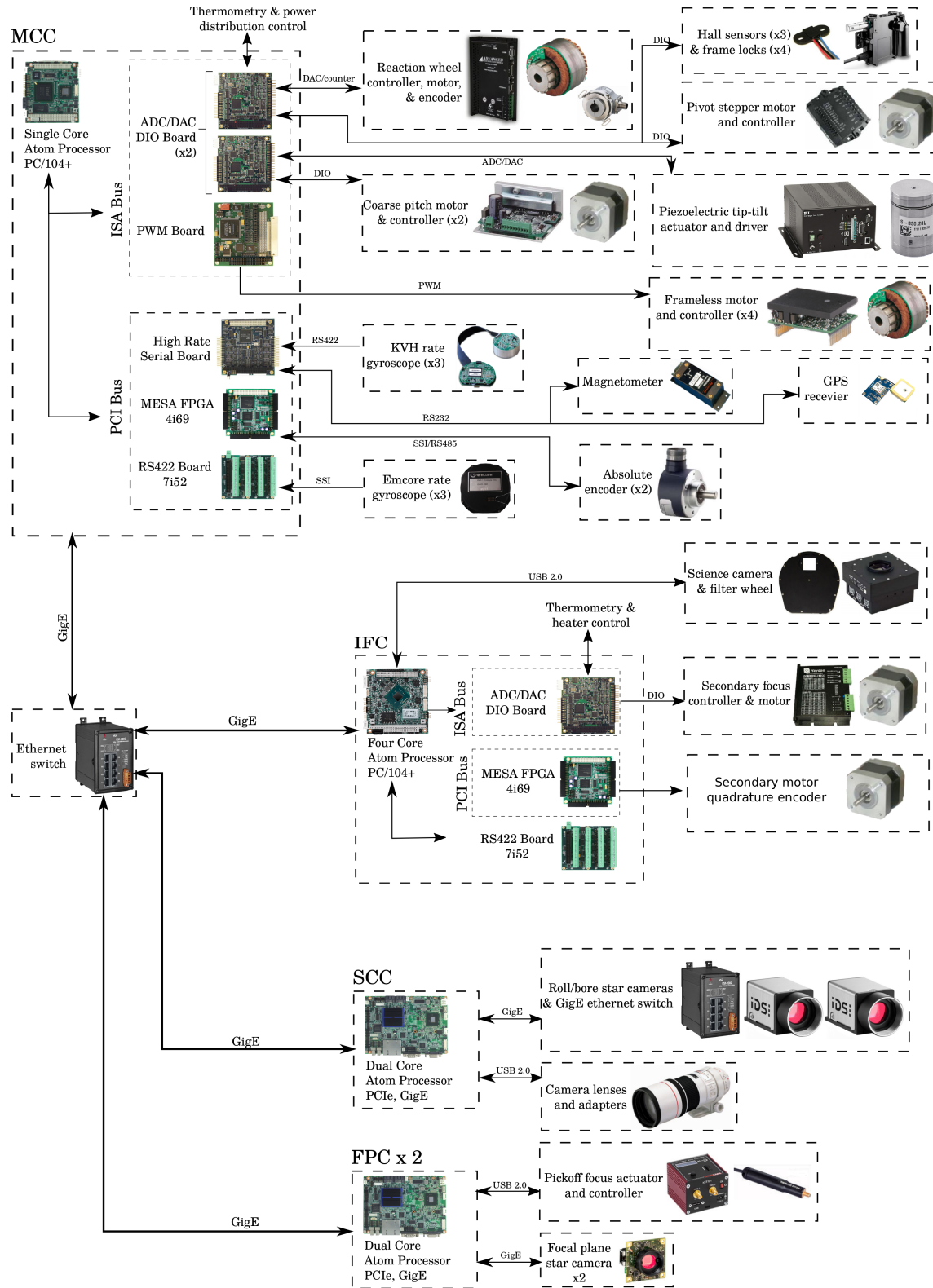


Figure 3.1: BIT computer and electronics layout for 2019 flight.

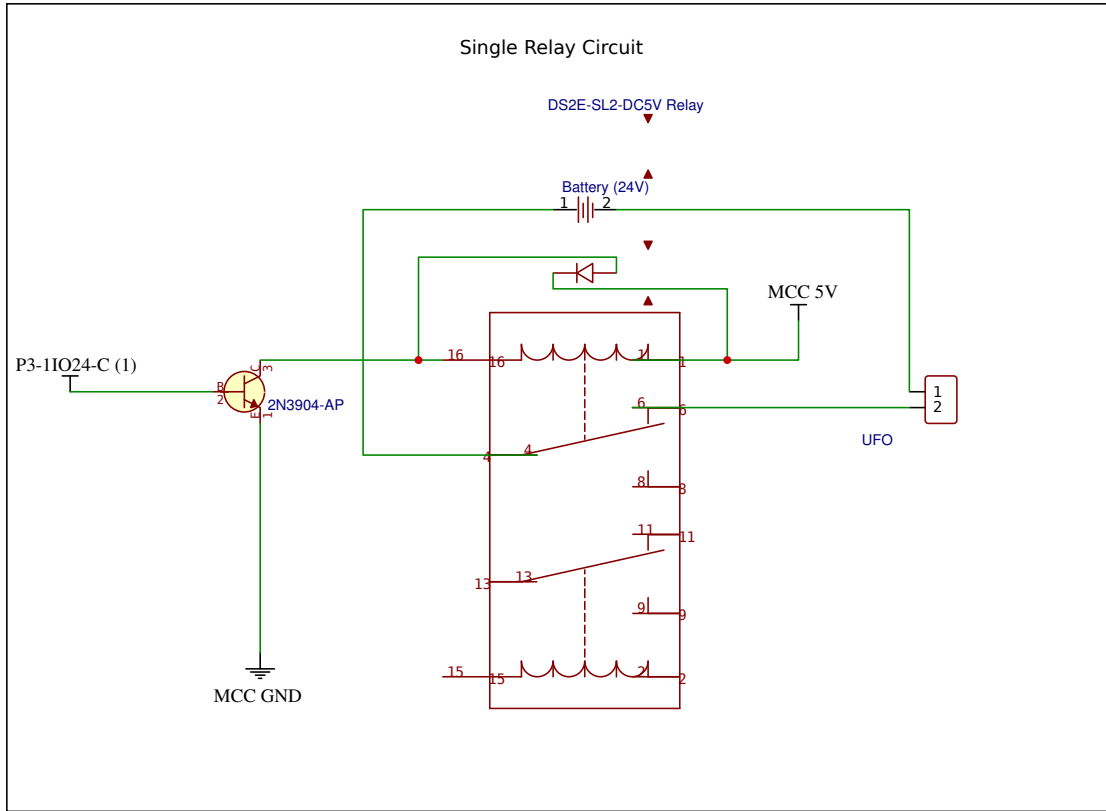


Figure 3.2: UFO system power control circuit. P3-IO24-C is a sample FPGA output that is fed into a transistor, when the output is pulsed the relay latches on/off turning on the UFO. The UFO is connected directly to SuperBIT’s 24V battery system while the relay is isolated and controlled by a 5V power system from the MCC.

3.3 UFO System

During flight SuperBIT data is nominally transmitted to the ground via satellite communication. Time streams are sent down over each of the available links (1 MBit LOS, 100 kbps High Gain TDRSS, Iridium) to a central ground computer. Non of the available links are sufficiently fast to transmit SuperBIT’s science date during the flight and therefore a hard drive recovery is required. For a ULDB flight there is a chance that SuperBIT will land in the ocean and thus be unrecoverable. In that scenario the hard drives need to be dropped mid flight separately from the primary payload. The hard drives are parachuted down in a raspberry pi controlled compartment known as the UFO system. This system required the design and building of a power control circuit that enables turning on multiple UFOs on and off separately. The design can be seen in Figure 3.2. The implementation was soldering 5 copies of the designed circuit in parallel in order to control 3x UFOs and 1x UFO wifi system. The circuit is a simple latched relay circuit controlled via bit output from the MESA FPGA in the MCC.

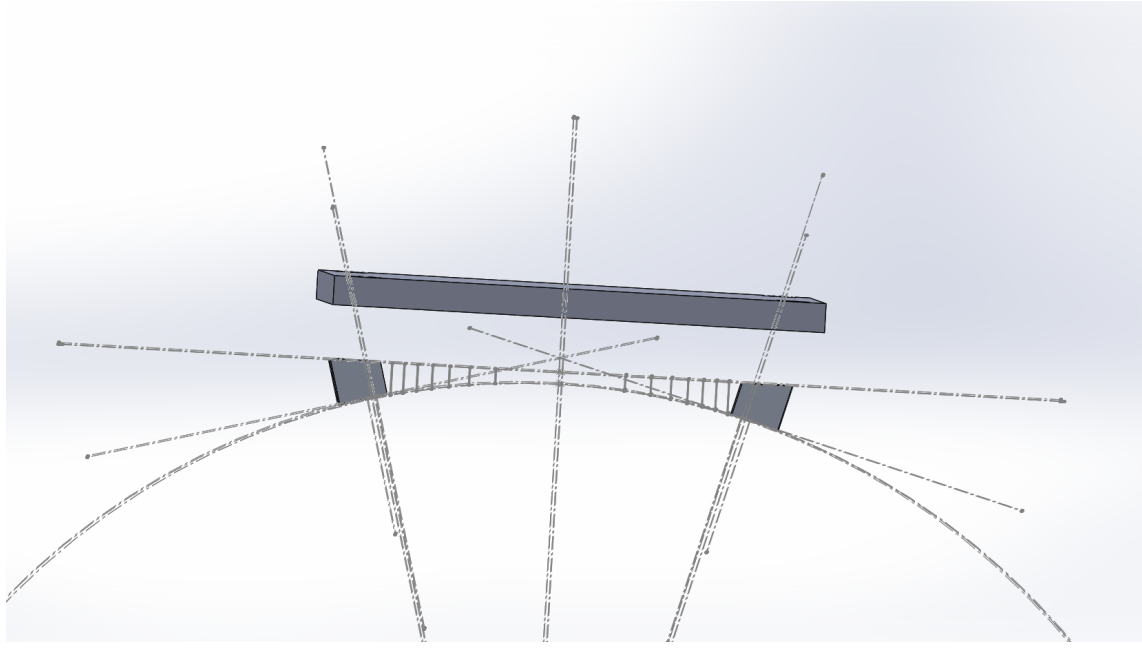


Figure 3.3: Baffle mounting system as designed on solidworks. Four angled aluminum feet are mounted directly to the baffle, the feet are angled such that a carbon fibre hex plate can lay flat on all four feet acting as a parallel surface to the telescope baffle's curvature.

3.4 Secondary Motors

The SuperBIT optical system is partially controlled by altering the position of the secondary mirror using three actuators providing tip/tilt/focus motion. The actuators needed to be understood and then have control software written for them. In order to understand the actuators we ran some tests and found the following features. A quadrature encoder is used to feedback position with 8000 encoder ticks per stepper motor revolution. A hall sensor is triggered as a limit switch to enable encoder calibration as well as indicate when the motor has reached min position. After characterizing the behavior of the motors VHDL code was written in order to enable the MESA FPGA in the IFC to interpretate raw encoder data, C wrapper was written to read the fpga write out from the PCI address and have the data available for control feedback.

3.5 Baffle Mounting Device

The star cameras and gyroscopes needed to mount onto the telescope baffle, as a result a mechanism to provide flat mounting surface on the telescope needed to be developed. The primary concern in the design process is to ensure that the mechanism is sufficiently stiff such that no vibrational modes are induced in the telescope and thus increasing the uncertainty in our pointing. We used sorbathane to dampen any vibrations as well as carbon fibre hex to ensure light and stiff material is used. The design can be seen in Figure 3.3.

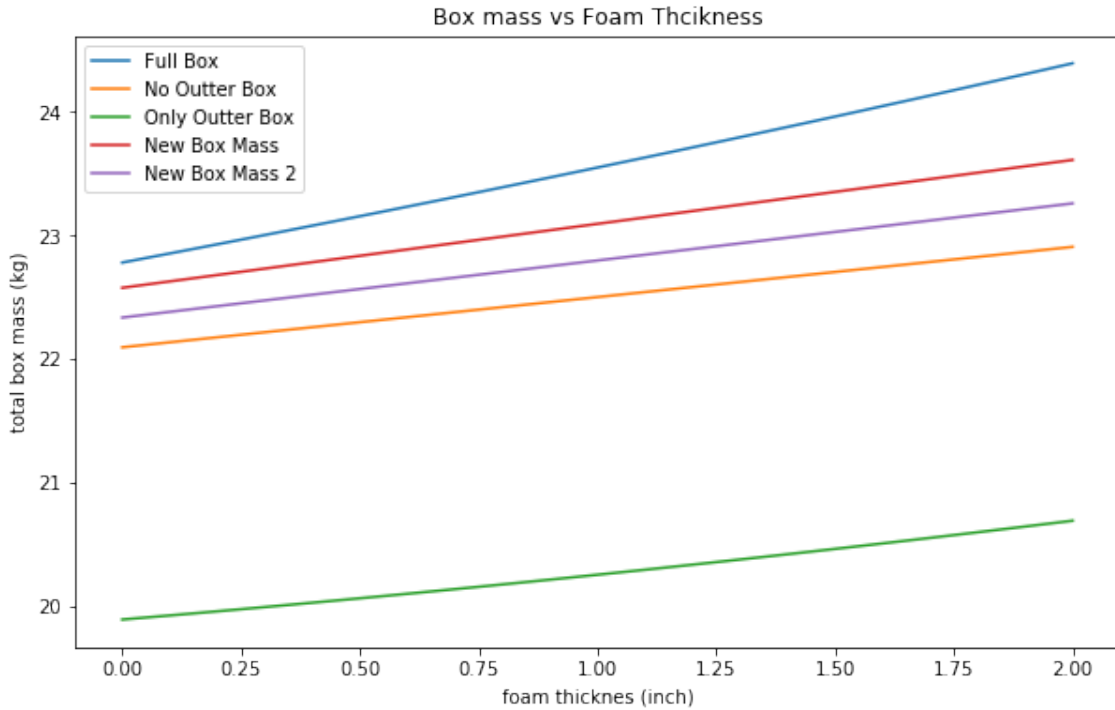


Figure 3.4: The mass of the thermal isolation box as a function of insulation foam thickness

3.6 Battery Boxes

SuperBIT uses lithium ion batteries that would permanently lose capacity if they drop below a critical temperature and therefore must be thermally controlled. During previous test flights it was empirically found that keeping BIT batteries at the functional temperature used a significant percentage of BIT's total power budget. As a result a new thermal insulation strategy was needed. A brief mathematical analysis was done and found that 2inch thick insulation foam in a heated aluminum box would be sufficient. Some plots for the analysis can be seen at Figure 3.4 Figure 3.5. The main considerations where the mass of the insulation box and power insulation.

Due to the location of the batteries it was found that the new insulation box will require a reduction in the reaction wheel size. A calculation was done to determine the loss in moment of inertia due to the presence of the battery boxes, we found that a total loss of 32% will be suffered. As a result a new heavier reaction wheel was designed to compensate for the loss. A summary of the analysis is seen in Figure 3.6

3.7 Inner Frame Design

A complete redesign of the BIT electronics layout on the inner frame was completed in order to optimize for space and cable use with respect to the new telescope. This involved the design of new mounting mechanisms for all flight computers and electronics as well as reordering position to optimize for mass balance.

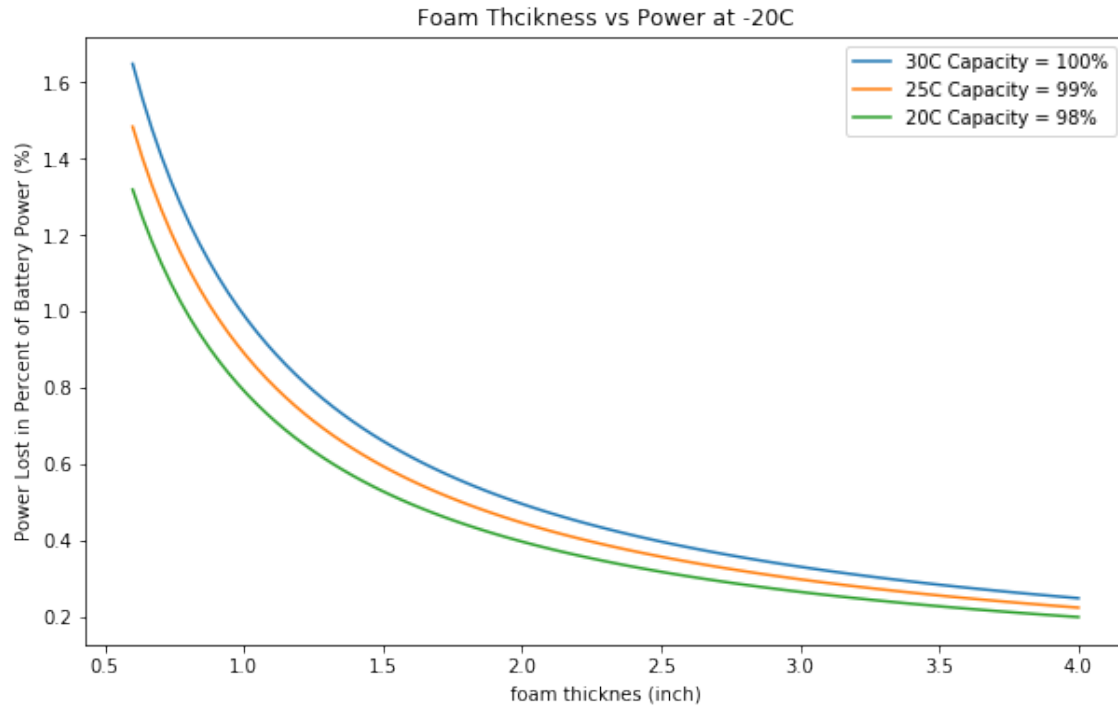


Figure 3.5: Thermal power lost in units of battery power percentage as a function of insolation foam thickness.

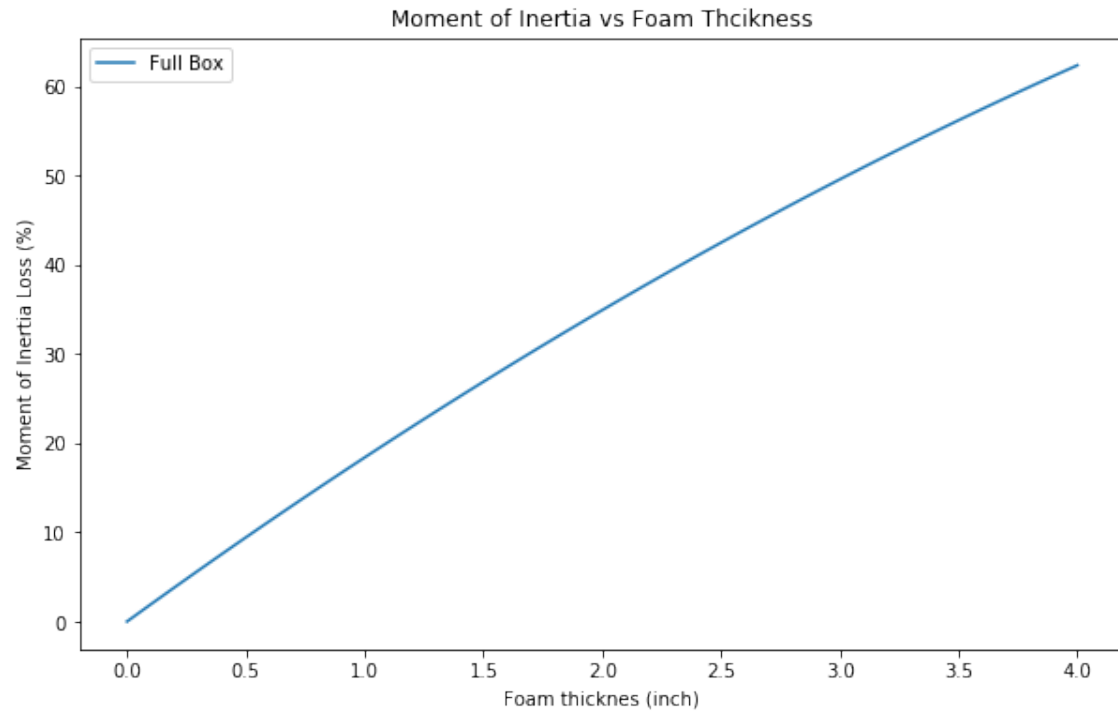


Figure 3.6: Loss of moment of inertia of the reaction wheel as a function of insolation foam thickness

Bibliography

- [1] The nobel prize in physics 2011 - advanced information. [nobelprize.org.](http://nobelprize.org/), 2014.
- [2] P. A. R. Ade et al. Planck 2013 results. I. Overview of products and scientific results. *Astron. Astrophys.*, 571:A1, 2014.
- [3] K. Bandura, G. E. Addison, M. Amiri, J. R. Bond, D. Campbell-Wilson, L. Connor, J.-F. Cliche, G. Davis, M. Deng, N. Denman, M. Dobbs, M. Fandino, K. Gibbs, A. Gilbert, M. Halpern, D. Hanna, A. D. Hincks, G. Hinshaw, C. Höfer, P. Klages, T. L. Landecker, K. Masui, J. Mena Parra, L. B. Newburgh, U.-l. Pen, J. B. Peterson, A. Recnik, J. R. Shaw, K. Sigurdson, M. Sitwell, G. Smecher, R. Smegal, K. Vanderlinde, and D. Wiebe. Canadian Hydrogen Intensity Mapping Experiment (CHIME) pathfinder. In *Ground-based and Airborne Telescopes V*, volume 9145, page 914522, July 2014.
- [4] Matthias Bartelmann and Matteo Maturi. Weak gravitational lensing. 2016.
- [5] Daniel J. Eisenstein et al. Detection of the Baryon Acoustic Peak in the Large-Scale Correlation Function of SDSS Luminous Red Galaxies. *Astrophys. J.*, 633:560–574, 2005.
- [6] H. Hoekstra. Weak gravitational lensing. *Proc. Int. Sch. Phys. Fermi*, 186:59–100, 2014.
- [7] H. Hoekstra and B. Jain. Weak Gravitational Lensing and Its Cosmological Applications. *Annual Review of Nuclear and Particle Science*, 58:99–123, November 2008.
- [8] David W. Hogg. Distance measures in cosmology. 1999.
- [9] Konrad Kuijken. The Basics of Lensing. *arXiv e-prints*, pages astro-ph/0304438, Apr 2003.
- [10] Rachel Mandelbaum. Weak Lensing for Precision Cosmology. *Annual Review of Astronomy and Astrophysics*, 56:393–433, Sep 2018.
- [11] Richard Massey, Henk Hoekstra, Thomas Kitching, Jason Rhodes, Mark Cropper, Jérôme Amiaux, David Harvey, Yannick Mellier, Massimo Meneghetti, Lance Miller, Stéphane Paulin-Henriksson, Sandrine Pires, Roberto Scaramella, and Tim Schrabback. Origins of weak lensing systematics, and requirements on future instrumentation (or knowledge of instrumentation). *mnras*, 429:661–678, Feb 2013.
- [12] Yannick Mellier. Probing the universe with weak lensing. *Ann. Rev. Astron. Astrophys.*, 37:127–189, 1999.

- [13] G. Meylan, P. Jetzer, P. North, P. Schneider, C. S. Kochanek, and J. Wambsganss, editors. *Gravitational Lensing: Strong, Weak and Micro*, 2006.
- [14] P. J. E. Peebles and Bharat Ratra. The Cosmological constant and dark energy. *Rev. Mod. Phys.*, 75:559–606, 2003.
- [15] A.W. Peet. General Relativity Notes . page <https://ap.io/483f/files/gr1.pdf>, 2018.
- [16] B. Ryden. *Introduction to Cosmology*. Cambridge University Press, 2016.
- [17] P. Schneider. *Extragalactic Astronomy and Cosmology*. 2006.
- [18] David H. Weinberg, Michael J. Mortonson, Daniel J. Eisenstein, Christopher Hirata, Adam G. Riess, and Eduardo Rozo. Observational probes of cosmic acceleration. *physrep*, 530:87–255, Sep 2013.